

Electric-field-induced nematic-cholesteric transition and three-dimensional director structures in homeotropic cells

I. I. Smalyukh,* B. I. Senyuk, P. Palffy-Muhoray, and O. D. Lavrentovich

Liquid Crystal Institute and Chemical Physics Interdisciplinary Program, Kent State University, Kent, Ohio 44242, USA

H. Huang and E. C. Gartland, Jr.

Department of Mathematical Sciences, Kent State University, Kent, Ohio 44242, USA

V. H. Bodnar, T. Kosa, and B. Taheri

AlphaMicron Inc., Kent, Ohio 44240, USA

(Received 3 October 2005; published 30 December 2005)

We study the phase diagram of director structures in cholesteric liquid crystals of negative dielectric anisotropy in homeotropic cells of thickness d which is smaller than the cholesteric pitch p . The basic control parameters are the frustration ratio d/p and the applied voltage U . Upon increasing U , the direct transition from completely unwound homeotropic structure to the translationally invariant configuration (TIC) with uniform in-plane twist is observed at small $d/p \lesssim 0.5$. Cholesteric fingers that can be either isolated or arranged periodically occur at $0.5 \lesssim d/p < 1$ and at the intermediate U between the homeotropic unwound and TIC structures. The phase boundaries are also shifted by (1) rubbing of homeotropic substrates that produces small deviations from the vertical alignment; (2) particles that become nucleation centers for cholesteric fingers; (3) voltage driving schemes. A novel reentrant behavior of TIC is observed in the rubbed cells with frustration ratios $0.6 \lesssim d/p \lesssim 0.75$, which disappears with adding nucleation sites or using modulated voltages. In addition, fluorescence confocal polarizing microscopy (FCPM) allows us to directly and unambiguously determine the three-dimensional director structures. For the cells with strictly vertical alignment, FCPM confirms the director models of the vertical cross sections of four types of fingers previously either obtained by computer simulations or proposed using symmetry considerations. For rubbed homeotropic substrates, only two types of fingers are observed, which tend to align along the rubbing direction. Finally, the new means of control are of importance for potential applications of the cholesteric structures, such as switchable gratings based on periodically arranged fingers and eyewear with tunable transparency based on TIC.

DOI: [10.1103/PhysRevE.72.061707](https://doi.org/10.1103/PhysRevE.72.061707)

PACS number(s): 42.70.Df, 61.30.Gd, 64.70.Md, 61.30.Jf

I. INTRODUCTION

The unique electro-optic and photonic properties of cholesteric liquid crystals (CLCs) make them attractive for applications in displays, switchable diffraction gratings, eyeglasses with voltage-controlled transparency, for temperature visualization, for mirrorless lasing, in beam steering and beam shaping devices, and many others [1–14]. In nearly all of these applications, CLCs are confined between flat glass substrates treated to set the orientation of molecules at the liquid crystal (LC)-glass interface along some well-defined direction (called the easy axis) and an electric field is often used to switch between different textures. In the confined CLCs, the magnitude of the free energy terms associated with elasticity, surface anchoring, and coupling to the applied field are frequently comparable: their competition results in a rich variety of director structures that can be obtained by appropriate surface treatment, material properties of CLCs, and applied voltage. Understanding these structures and the transitions between them is of great practical interest and of fundamental importance [12–14].

CLCs have a twisted helicoidal director field in the ground state. The axis of molecular twist is called the helical

axis and the spatial period over which the liquid crystal molecules twist through 2π is called the cholesteric pitch p . CLCs can be composed of a single compound or of mixtures of a nematic host and one or more chiral additives. Cholesterics usually have the equilibrium pitch p in the range 100 nm–100 μ m; the pitch p can be easily modified by additives. When CLCs are confined in the cells with different boundary conditions or subjected to electric or magnetic fields, one often observes complex three-dimensional (3D) structures. The cholesteric helix can be distorted or even completely unwound by confining CLCs between two substrates treated to produce homeotropic boundary conditions [15]. Interest in this subject was initiated by Cladis and Kleman [16], subsequently a rich variety of spatially periodic and uniform structures have been reported [15,17–30]. These structures can be controlled by varying the cell gap thickness d , pitch p , applied voltage U , and the dielectric and elastic properties of the used CLC. The complexity of many LC structures usually does not allow simple analytic descriptions of the director configuration. Since the pioneering work of Press and Arrott [19,20], a great progress has been made in computer simulations of static director patterns in CLCs confined into homeotropic cells (see, for example, [15,17–19,21–23]), which brought much of the current understanding of these structures.

*Corresponding author. Email address: smalyukh@lci.kent.edu

The first goal of this work is to study phase diagram and director structures that appear because of geometrical frustration of CLCs in the cells with either strictly vertical or slightly tilted ($<2^\circ$) easy axis at the confining substrates. We start with the phase diagram in the plane of $\rho=d/p$ and U similar to the one reported in Refs. [15,24] and then proceed by studying influence of such extra parameters as rubbing, introducing nucleation sites, and voltage driving schemes. We use CLCs with negative dielectric anisotropy; the applied voltages are sufficiently low and the frequencies are sufficiently high to avoid hydrodynamic instabilities [12]. Cell gap thicknesses d are smaller than p and the phase diagrams are explored for frustration ratios $\rho=0-1$ and $U=(0-4)V_{rms}$. For small ρ and U , the boundary conditions force the LC molecules throughout the sample to orient perpendicular to the glass plates. Above the critical values of ρ and/or U , cholesteric twisting of the director takes place [15]. Depending on ρ , U , and other conditions, the twisted director structures can be either uniform or spatially periodic, with a wave vector in the plane of the cell. Upon increasing U for $\rho<0.5$, the direct transition from completely unwound homeotropic structure to the translationally invariant configuration TIC [15,19,20] with uniform in-plane twist is observed. Cholesteric fingers (CFs) of different types that can be either isolated or arranged periodically are observed for $0.5 \lesssim \rho < 1$ and intermediate U between the homeotropic unwound and TIC structures. The phase diagrams change if the homeotropic alignment layers are rubbed, if particles that become the nucleation centers for CFs are present, and if different driving voltage schemes are used. Upon increasing U in rubbed homeotropic cells with $0.6 < \rho < 0.75$, we observe a reentrant behavior of TIC and the following transition sequence: (1) homeotropic untwisted state, (2) translationally invariant twisted state, (3) periodic fingers structure, and (4) translationally invariant twisted state with larger in-plane twist. This sequence has not been observed in our own and in the previously reported [15] studies of unrubbed homeotropic cells.

The second goal of this work is to unambiguously reconstruct director field of CFs and other observed structures in the phase diagram. For this we use the fluorescence confocal polarizing microscopy (FCPM) [31]. Although the fingers of different types look very similar under the polarizing microscope (which may explain some confusion in the literature [23]), FCPM allows clear differentiation of CFs, as well as other structures. We directly visualize the TIC with the total director twist ranging from 0 to 2π , depending on ρ and U , and rubbing. We reconstruct director structure in the vertical cross sections of four different types of CFs that are observed for cells with strictly vertical alignment. We unambiguously prove the models described recently by Oswald *et al.* [15], while disproving some of the other models that were proposed in the early literature (see, for example, [23]). Only two types of CF structures are observed in CLCs confined to cells with slightly tilted easy axes at the substrates.

The third goal of our work stems from the importance of the studied structures for practical applications. The spatially uniform TIC and homeotropic-to-TIC transition are used in the electrically driven light shutters, intensity modulators, eyewear with tunable transparency, and displays [1,5,6,8]. In

these applications, it is often advantageous to work in the regime of high ρ , but fingers are not desirable since they scatter light. In our study, we, therefore, focus on obtaining maximum effect of different factors on the phase diagrams. We demonstrate that the combination of rubbing and low-frequency voltage modulation can stabilize the uniformly twisted structures up to $\rho \approx 0.75$, much larger than $\rho \approx 0.5$ reported previously [15]. The presence of nucleation centers, such as particles used to set the cell thickness, tends to destroy the homogeneously twisted cholesteric structure even at relatively low $\rho \approx 0.5$ confinement ratios; this information is important for the optimal design of the finger-free devices. On the other hand, periodic finger patterns with well controlled periodicity and orientation may be used as voltage-switchable diffraction gratings. Our finding, which enables the very possibility of such application, is that rubbing can set the unidirectional orientation of periodically arranged fingers.

The paper is organized as follows. We describe materials, cell preparation, and experimental techniques in Sec. II. The phase diagrams are described in Sec. III A and the reconstructed director structures in Sec. III B. Section IV gives an analytical description of the transition from homeotropic to a twisted state as well as a brief discussion of other structures and transitions along with their potential applications. The conclusions are drawn in Sec. V.

II. EXPERIMENT

A. Materials and cell preparation

The cells with homeotropic boundary conditions were assembled using glass plates coated with transparent indium tin oxide (ITO) electrodes and the polyimide JALS-204 (purchased from JSR, Japan) as an alignment layer. JALS-204 provides strong homeotropic anchoring; anchoring extrapolation length, defined as the ratio of the elastic constant to the anchoring strength, is estimated to be in the submicron range. Some of the substrates with thin layers of JALS-204 were unidirectionally buffed (five times using a piece of velvet cloth) in order to produce an easy axis at a small angle γ to the normal to the cell substrates. γ was measured by conoscopy and magnetic null methods [32]. The value of γ weakly depends on the rubbing strength, but in all cases it was small, $\gamma < 2^\circ$. The cell gap thickness was set using either the glass microsphere spacers uniformly distributed within the area of a cell (one spacer per approximately $100 \mu\text{m} \times 100 \mu\text{m}$ area) or strips of mylar film placed along the cell edges. The cell gap thickness d was measured after cell assembly using the interference method [33] with a LAMBDA18 (Perkin Elmer) spectrophotometer. In order to study textures as a function of the confinement ratio $\rho=d/p$, we constructed a series of cells, with identical thickness, but filled with CLCs of different pitch p . To minimize spherical aberrations in the FCPM, observations were made with immersion oil objectives, using glass substrates of thickness 0.15 mm with refractive index 1.52 [31]. Regular (1 mm) and thick (3 mm) substrates were used to construct cells for polarizing microscopy (PM) observations.

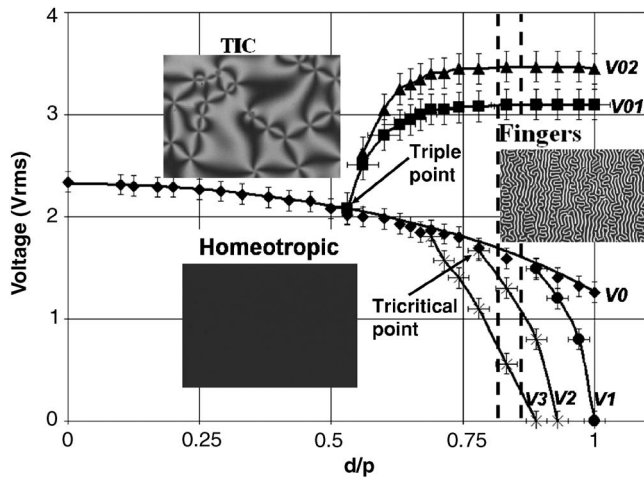


FIG. 1. Phase diagram of structures in the U - ρ parameter space for CLCs in cells with homeotropic surface anchoring. The boundary lines $V0$ - $V3$, $V01$, $V02$ separate different phases (cholesteric structures). The two dashed vertical lines mark $\rho_{triple}=0.816$ and $\rho_{tricritical}=0.861$ as estimated according to Ref. [24] for the material parameters of AMLC-0010-ZLI-811 LC mixture. The solid line $V0$ was calculated using Eq. (1) and parameters of the used CLC; the solid lines $V1$ - $V3$, $V01$, $V02$ connect the experimental points to guide the eye.

Cholesteric mixtures were prepared using the nematic host AMLC-0010 (obtained from AlphaMicron Inc., Kent, Ohio) and the chiral additive ZLI-811 (purchased from EM Industries). The helical twisting power $P_{HT}=10.47 \mu\text{m}^{-1}$ of the additive ZLI-811 in the AMLC-0010 nematic host was determined using the method of Grandjean-Cano wedge [34,35]. The obtained mixtures had pitch $2 < p < 500 \mu\text{m}$ as calculated from $p=1/(c_{chiral} \times P_{HT})$ where c_{chiral} is the weight concentration of the chiral agent, and verified by the Grandjean-Cano wedge method [34,35,37]. The low frequency dielectric anisotropy of the AMLC-0010 host is $\Delta\epsilon = -3.7$ ($\epsilon_{\parallel}=3.4, \epsilon_{\perp}=7.1$) as determined from capacitance measurements for homeotropic and planar cells using a SI-1260 impedance/gain-phase analyzer (Schlumberger) [1,38]. The birefringence of AMLC-0010 is $\Delta n=0.078$ as measured with an Abbe refractometer. The elastic constants describing the splay, twist, and bend deformations of the director in AMLC-0010 are $K_{11}=17.2pN$, $K_{22}=7.51pN$, $K_{33}=17.9pN$ as determined from the thresholds of electric and magnetic Freedericksz transition in different geometries [1,38]. The cholesteric mixtures were doped with a small amount of fluorescent dye *n,n'*-bis(2,5-di-tert-butylphenyl)-3,4,9,10-perylene-dicarboximide (BTBP) [31] for the FCPM studies. Small quantities (0.01 wt. %) of BTBP dye were added to the samples; at these concentrations, the dye is not expected to affect properties of the CLCs used in our studies.

Constant amplitude and modulated amplitude signals were applied to the cells using a DS345 generator (Stanford Research Systems) and a Model 7602 wide-band amplifier (Krohn-Hite), which made possible the use of a wide range of carrier and modulation frequencies (10–100 000 Hz). The transitions from the homeotropic untwisted to a variety of twisted structures were monitored via capacitance measure-

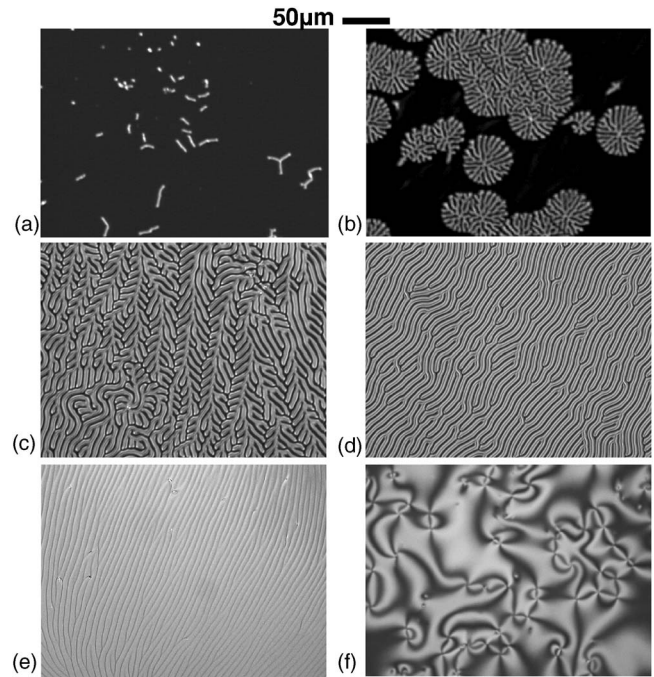


FIG. 2. Polarizing microscope textures observed in different regions of the phase diagram of structures shown in Fig. 1: (a) isolated CFs coexisting with the homeotropic untwisted state between the boundary lines $V1$ and $V2$ of Fig. 1; (b) dendriticlike growth of CFs (observed between the boundary lines $V0$ and $V1$); (c) branching of CFs with increasing voltage, between the boundary lines $V0$ and $V1$; (d) periodically arranged CFs where the individual CFs are separated by homeotropic narrow stripes, observed between $V0$ and $V01$; (e) CFs merge producing undulating TIC, observed between $V01$ and $V02$; (f) TIC with umbilics, observed above the lines $V0$ and $V02$. Picture shown in part (b) was taken about 2 s after voltage was applied; it shows an intermediate state in which the circular domains grow from nucleation sites and will eventually fill in the whole area of the cell by the fingers.

ments and by measuring the light transmittance of the cell between crossed polarizers. The transitions between different director structures and textures were characterized with PM and FCPM [31] as described below.

B. Polarizing microscopy and fluorescence confocal polarizing microscopy

Polarizing microscopy observations were performed using the Nikon Eclipse E600 microscope with the Hitachi HV-C20 charge-coupled device (CCD) camera. The PM studies were also performed using a BX-50 Olympus microscope in the PM mode. In order to directly reconstruct the vertical cross sections of the cholesteric structures, we performed further studies in the FCPM mode of the very same modified BX-50 microscope [31] as described below. The PM and FCPM techniques are used in parallel and provide complementary information.

The FCPM setup was based on a modified BX-50 fluorescence confocal microscope [31]. The excitation beam ($\lambda = 488 \text{ nm}$, from an Ar laser) is focused by an objective onto a small submicron volume within the CLC cell. The fluores-

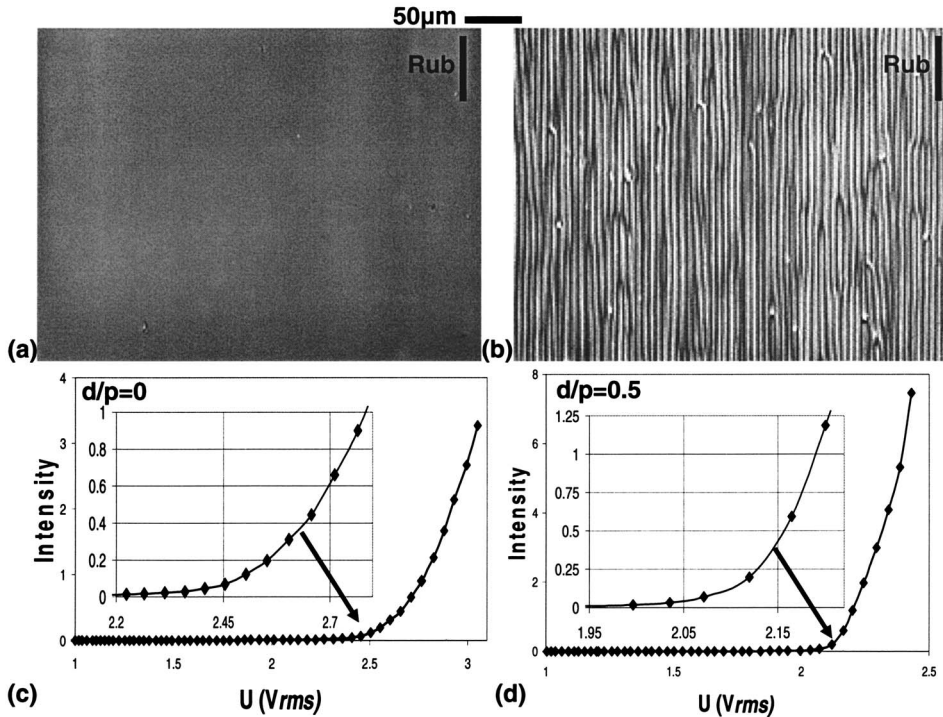


FIG. 3. (a), (b) Polarizing microscope textures of (a) the TIC with no umbilics and (b) periodic fingers pattern in a homeotropic cell with one of the substrates rubbed along the black bar. (c), (d) Light transmission through the cell with rubbed homeotropic substrates placed between crossed polarizers for (c) $\rho=0$ and (d) $\rho=0.5$. The insets in (c), (d) show details of intensity changes in the vicinity of homeotropic-TIC transition; note that the rubbing-induced pretilt makes these dependencies not as sharp as those normally observed in nonrubbed homeotropic cells (see, for example, Ref. [40]).

cent light from this volume is detected by a photomultiplier in the spectral region 510–550 nm. A pinhole is used to discriminate against emission from the regions above and below the selected volume. The pinhole diameter D is adjusted according to magnification and numerical aperture (NA) of the objective; $D=100 \mu\text{m}$ for an immersion oil $60\times$ objective with $\text{NA}=1.4$. A very same polarizer is used to determine the polarization of both the excitation beam and the detected fluorescent light collected in the epifluorescence mode. The relatively low birefringence ($\Delta n \approx 0.078$) of the AMLC-0010 nematic host mitigates two problems that one encounters in FCPM imaging of CLCs: (1) defocussing of the extraordinary modes relative to the ordinary modes [31] and (2) the Mauguin effect, where polarization follows the twisting director field [18,39].

The used BTBP dye has both absorption and emission transition dipoles parallel to the long axis of the molecule [34,36,37]. The FCPM signal, resulting from a sequence of absorption and emission events, strongly depends on the angle β between the transition dipole moment of the dye (assumed to be parallel to the local director \hat{n}) and the polarization \hat{P} . The intensity scales as $I_{FCPM} \sim \cos^4 \beta$, [31] as both the absorption and emission are proportional to $\cos^2 \beta$. The strongest FCPM signal corresponds to $\hat{n} \parallel \hat{P}$, where $\beta = 0$, and sharply decreases when β becomes nonzero [18,31,34,37]. By obtaining the FCPM images for different \hat{P} , we reconstruct director structures in both in-plane and vertical cross sections of the cell from which then the entire 3D director pattern is reconstructed. We note that in the FCPM images, the registered fluorescence signal from the bottom of the cell can be somewhat weaker than from the top, as a result of light absorption, light scattering caused by director fluctuations, depolarization, and defocussing. To mitigate these experimental artifacts and to maintain both

axial and radial resolution within $1 \mu\text{m}$, we used relatively shallow ($\leq 20 \mu\text{m}$) scanning depths [18,31]. The other artifacts, such as light depolarization by a high NA objective, are neglected as they are of minor importance [18,31,34,37].

III. RESULTS

A. Phase diagrams of textures and structures

We start with an experimental phase diagram of cholesteric structures in the homeotropic cells similar to the one

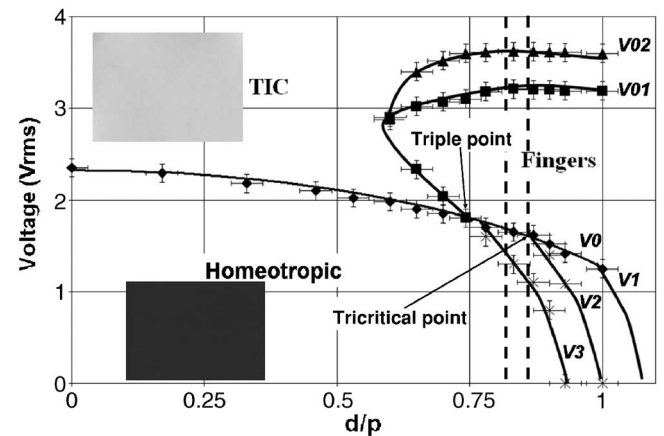


FIG. 4. Phase diagram of structures in the U vs ρ parameter space for CLCs in the cells with homeotropic boundary conditions and substrates rubbed in antiparallel directions. The cell has mylar spacers at the edges; no spacer particles are present in the bulk. The lines $V0-V3$, $V01$, $V02$ separate different phases and the two dashed vertical lines mark $\rho_{\text{triple}}=0.816$ and $\rho_{\text{tricritical}}=0.861$ corresponding to the triple and tricritical points, similar to Fig. 1. The solid line $V0$ was calculated using Eq. (1) and is the same as in Fig. 1; the solid lines $V1-V3$, $V01$, $V02$ connect the experimental points to guide the eye.

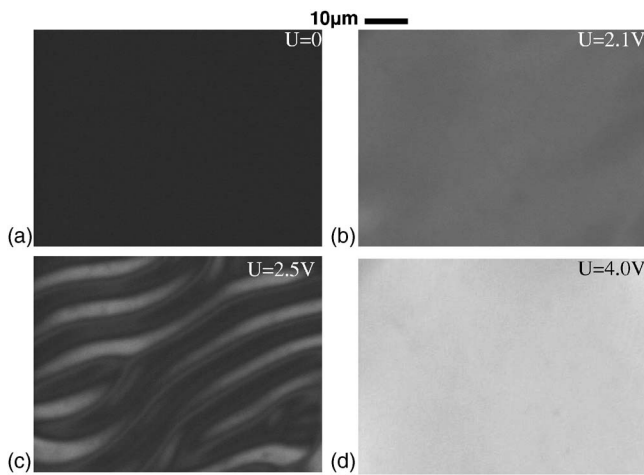


FIG. 5. Polarizing microscope textures illustrating the transition from (a) homeotropic untwisted state to (b) TIC with no umbilics and total twist $\Delta\phi \approx \pi$ between the substrates, and then to (c) fingers pattern that slowly (~ 1 s) appears from TIC, and then to (d) uniform TIC with $\approx 2\pi$ twist. The applied voltages are indicated. The homeotropic cell has substrates rubbed in antiparallel directions; $\rho=0.65$. The cell was assembled by using mylar spacers at the cell edges; no particles or other nucleation sites are present in the working area of the cell.

reported in [15,24] and then explore how this diagram is affected by rubbing of homeotropic substrates, using different voltage driving schemes, and introducing nucleation sites. We note that for pitch $p \gtrsim 5 \mu\text{m}$ and the cell gap $d \gtrsim 5 \mu\text{m}$ much larger than the anchoring extrapolation length ($< 1 \mu\text{m}$, describing polar anchoring at the interface of CLC and JALS-204 layer), the observed structures depend on $\rho=d/p$ but not explicitly on d and p . We, therefore, construct the diagrams of structures in the plane of the applied voltage U and the frustration ratio ρ ; to describe the phase diagram, we adopt the terminology introduced in Ref. 15. The diagrams display director structures (phases) of homeo-

tropic untwisted state, isolated CFs and periodically arranged CFs, the TIC and the modulated (undulating) TIC. The phase boundary lines are denoted as $V0-V3$, $V01$, $V02$, see Fig. 1, similarly to Refs. [15,24] (for comparison with the phase diagrams reported for other LCs). As we show below, the phase diagram can be modified to satisfy requirements for several electro-optic applications of the CLC structures.

1. Cells with unrubbed homeotropic substrates

The diagram for unrubbed homeotropic cells is shown in Fig. 1. The completely unwound homeotropic texture is observed at small U and ρ , see Fig. 1. At high U above $V0$, $V01$, and $V02$, the TIC with some amount of director twist (up to 2π , helical axis along the cell normal) is observed; the twist in TIC is accompanied by splay and bend deformations. The TIC texture is homogeneous within the plane of a cell except that it often contains the so-called umbilics, defects in direction of the tilt [12], see Fig. 2(f). Periodically arranged CFs are observed for voltages $U \approx 1.5-3.5V_{rms}$ and for $0.5 < \rho < 1$, see Fig. 1 and Figs. 2(b)-2(e). If the values of U and ρ are between the $V0$ and $V01$ boundary lines (Fig. 1), a transient TIC appears first but then it is replaced (within 0.1-10 s after voltage pulse, depending on ρ and U) by a periodic pattern of CFs, which also undergoes slow relaxation; equilibrium is reached only in 3-50 s, see Fig. 2(d). The isolated CFs coexisting with the homeotropic state are observed at $U \approx 1.8$ and for $0.75 < \rho < 1$, see Fig. 1 and Figs. 2(a) and 2(b). For ρ and U between $V0$ and $V1$, the isolated fingers start growing from nucleation sites such as spacers [Fig. 2(b)], or from already existing fingers. In both cases, the CFs separated by homeotropic regions split in order to fill in the entire space with a periodic texture of period $\sim p$, similar to the one shown in Fig. 2(c). In the region between $V1$ and $V2$, isolated CFs nucleate and grow but they do not split and do not fill in the whole sample; fingers in this part of diagram coexist with homeotropic untwisted structure, see Fig. 2(a). Hysteresis is observed between the $V2$ and $V3$ lines: a homeotropic texture is observed if the voltage is

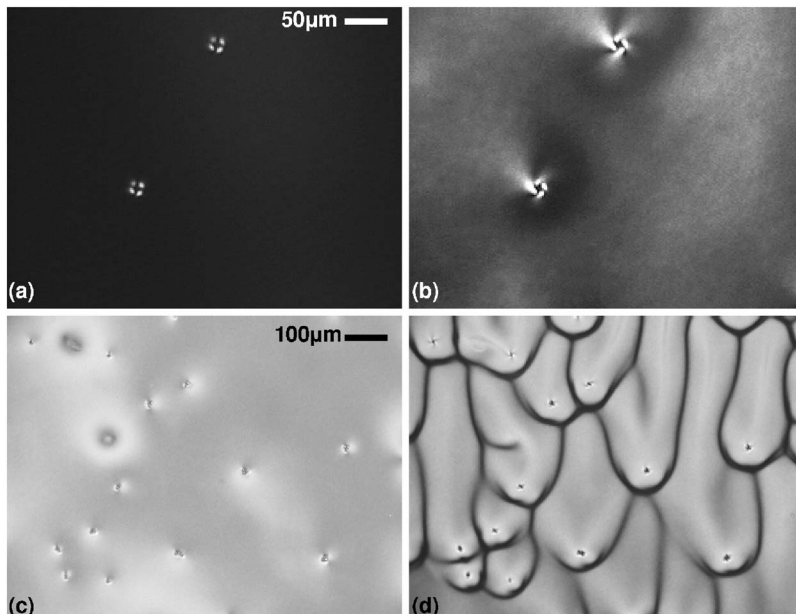


FIG. 6. Influence of spherical particles with perpendicular surface anchoring on the CLC structures in homeotropic cells: (a) particle-induced director distortions in the homeotropic state; (b) director distortions in the TIC at $U \approx U_{th}$; (c) TIC 10 ms after $U > U_{th}$ is applied; and (d) relaxation of the distortions in TIC via formation of fingers as observed ≈ 1 s after U is applied (the particles become nucleation sites for the fingers).

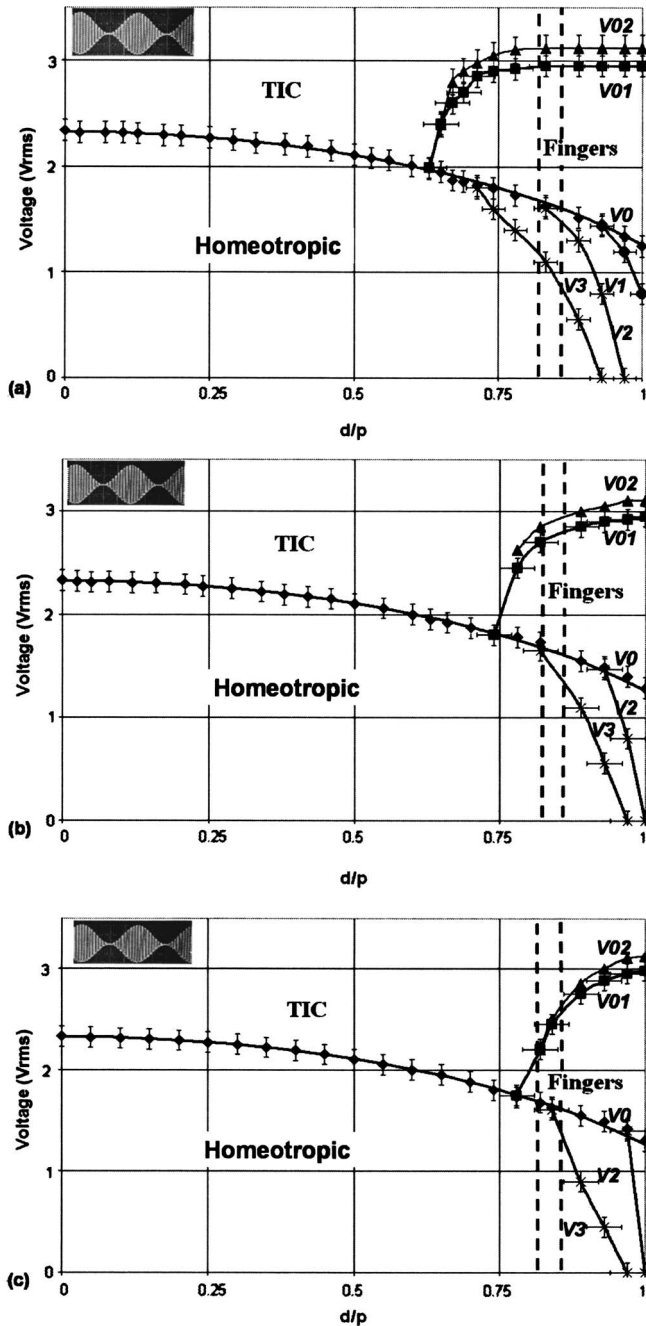


FIG. 7. Phase diagram of structures in the U vs ρ parameter space for CLCs in homeotropic cells with rubbed substrates: (a) antiparallel (i.e., at 180°), (b) at 90° , (c) at 270° . The frequency of the applied voltage is 1 kHz, which is amplitude-modulated with a 50 Hz sinusoidal signal. The boundary lines $V0-V3$, $V01$, $V02$ separate different phases and the two dashed vertical lines mark $\rho_{triple}=0.816$ and $\rho_{tricritical}=0.861$, similar to Figs. 1 and 4. The solid line $V0$ was calculated using Eq. (1) and is the same as in Figs. 1 and 4; the solid lines $V1-V3$, $V01$, $V02$ connect the experimental points to guide the eye.

increased, but isolated fingers coexisting with untwisted homeotropic structure can be found if U is decreased from the initial high values. Even though the neighboring CFs in the fingers pattern are locally parallel to each other [Figs. 2(c)

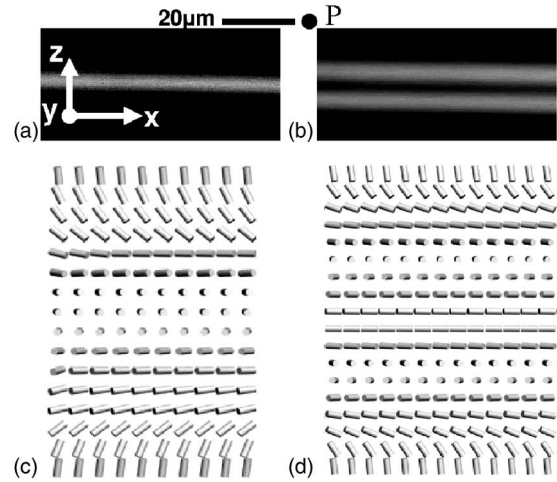


FIG. 8. FCPM cross sections (a), (b) and schematic of director structures (c), (d) of TIC with twist: (a), (c) $\approx \pi$ at $U=5 V_{rms}$ and $\rho=1/2$; (b), (d) $\approx 2\pi$ at $U=5 V_{rms}$ and $\rho=1$. The polarization of the probe light in FCPM marked by “P” is in the y direction, along the normal to the pictures in (a), (b).

and 2(d)], there is no preferential orientation of the fingers in the plane of the cell on the scales $\gtrsim 10$ mm. Finally, the periodic structure observed between $V01$ and $V02$ does not contain interspersed homeotropic regions, see Fig. 2(e). The director field of CFs as well as other structures of the diagram will be revealed by FCPM below, see Sec. III B.

The behavior of the voltage-driven transitions between untwisted homeotropic and different types of twisted structures is reminiscent of conventional temperature-driven phase transitions with voltage playing a role similar to temperature. The phase diagram of structures has a Landau tricritical point $\rho=\rho_{tricritical}$ at which $V2$ and $V0$ meet. The order of the transition changes from the second order (continuous) at $\rho<\rho_{tricritical}$ to the first order (discontinuous, proceeding via nucleation) at $\rho>\rho_{tricritical}$, see Fig. 1. The phase diagram also has a triple point at $\rho=\rho_{triple}$, where $V0$ and $V01$ meet. At the triple point, the untwisted homeotropic texture coexists with two different twisted structures, spatially uniform TIC and periodic fingers pattern. The phase diagram and transitions in homeotropic cells with perpendicular easy axes at the substrates are qualitatively similar to those reported by Oswald *et al.* [15,24] for other materials. Both qualitative and quantitative differences are observed when the homeotropic substrates are rubbed to produce slightly tilted easy axes at the confining substrates as discussed below.

2. Effects of rubbing and nucleation centers

Rubbing of the homeotropic alignment layers induces a small pretilt angle from the vertical axis, $\gamma<2^\circ$. The azimuthal degeneracy is, therefore, broken, and the projection of easy axis defines a unique direction in the plane of a cell. Therefore, even rubbing of only one of the cell substrates has a strong effect on the CLC structures: (1) no umbilics are observed in the TIC, see Fig. 3(a); (2) CFs preferentially align along the rubbing direction, see Fig. 3(b). In addition, the homeotropic-TIC transition, which is sharp in cells with

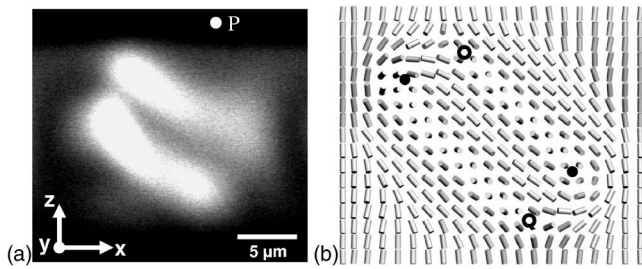


FIG. 9. FCPM vertical cross sections (a) and schematic of director structures (b) of a CF1-type isolated finger. The polarization of the probe light in FCPM marked by “P” is in the y direction, along the normal to the picture in (a). The nonsingular λ disclinations are marked by circles in (b); the open circles correspond to the $\lambda^{-1/2}$ and the solid circles correspond to the $\lambda^{+1/2}$ disclinations.

vertical alignment [40], becomes somewhat blurred for rubbed homeotropic substrates with small γ , see Figs. 3(c) and 3(d).

In principle, one can set opposite rubbing directions on the substrates; we report a phase diagram of structures for such antiparallel rubbing in Fig. 4. The cells used to obtain the diagram were constructed from thick 3-mm glass plates and only the mylar spacers at the cell edges were used to set the cell gap thickness. Compared to phase diagrams of structures with unrubbed substrates, dramatic changes are observed at $\rho \gtrsim 0.5$. The direct homeotropic to TIC transition is observed up to $\rho \approx 0.75$. The experimental triple and tricritical points are closer to each other than for unrubbed cells (compare Fig. 1 and Fig. 4). Interestingly, within the range $0.6 < \rho < 0.75$ and upon increasing U , one first observes a homogeneous TIC [Fig. 5(b)], which is then replaced by a periodic fingers pattern at higher U [Fig. 5(c)], and again a uniform TIC at even higher $U > 3-3.5$ V [Fig. 5(d)]. The same sequence, TIC-fingers-TIC-homeotropic, is also observed upon decreasing U from initial high values. Pursuing the analogy with temperature-driven phase transitions, the TIC texture between the fingers pattern and homeotropic texture can be considered as a reentrant TIC phase. As compared to unrubbed cells, the antiparallel rubbing has little effect on V_0 , but shifts the other boundary lines toward increasing ρ . The effects of antiparallel rubbing on the phase diagram can be explained as follows. At $\rho \sim 0.5$, antiparallel rubbing matches the director twist of TIC, which at high U is

$\approx \pi$. Therefore, TIC is stabilized by antiparallel rubbing and CFs do not appear until higher ρ , see Fig. 4.

The transient TIC disappears if large quantities of spacers ($> 100/\text{mm}^2$) or other nucleation sites for fingers are present in the cells with antiparallel rubbing; in this case, the phase diagram is closer to the one shown in Fig. 1. The spacers with perpendicular surface anchoring produce director distortions in their close vicinity even in the part of the diagram corresponding to the homeotropic unwound state, see Fig. 6(a). In the vicinity of the homeotropic-TIC transition [Fig. 6(b)], the director realignment starts in the vicinity of spacers. Similar to the observations in Refs. [27,41], particles with perpendicular surface anchoring cause inversion walls (IW) and disclinations. The TIC with $0.5 < \rho < 0.75$ [Fig. 6(c)] is eventually replaced by fingers, which are facilitated by the particles [Fig. 6(d)]. Moreover, even at high U , TIC remains spatially nonuniform and contains different types of IWs and disclination lines [27,41], which are caused by the boundary conditions at the surfaces of the particles.

3. Phase diagrams for different voltage driving schemes

The phase diagrams of structures shown in Figs. 1 and 4 were obtained with constant amplitude sinusoidal voltages applied to the cells. The diagram changes dramatically if the applied voltage is modulated. The effect is especially strong in the cells with rubbed homeotropic substrates, for which we present results in Figs. 7(a)–7(c); a somewhat weaker effect is also observed for unrubbed substrates. We explored modulation with rectangular-type, triangular, and sinusoidal signals of different duration and modulation depth. The strongest effect is observed with 100% modulation depth and sinusoidal modulation signal at frequencies (10–200 Hz). The fingers patterns are shifted toward increasing ρ , see Fig. 7. At the same time, the *rms* voltage values of homeotropic-TIC transition are practically the same for different voltage driving schemes, see Figs. 1, 4, and 7. We assume that the effect of amplitude modulation is related to the very slow dynamics of some of the structures (see Secs. III A 1 and III A 2), such as CFs; the corresponding parts of the diagram are the most sensitive to voltage driving schemes.

The substantial combined effect of rubbing and voltage driving schemes is important for practical applications of the homeotropic-TIC transition when it is important to have a strongly twisted, but finger-free field-on state [5,8]. We,

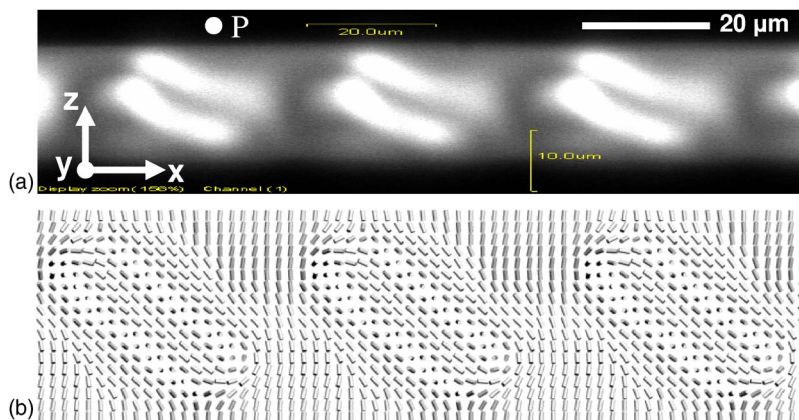


FIG. 10. (Color online) FCPM cross sections (a) and schematic of director structures (b) of a periodic finger pattern composed of CF1s separated by homeotropic stripes. The polarization of the FCPM probe light marked by “P” is normal to the picture in (a).

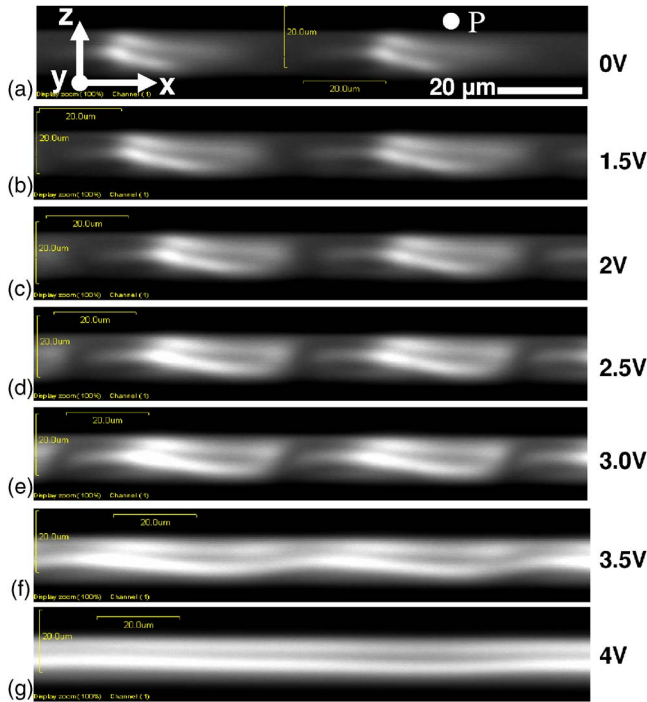


FIG. 11. (Color online) FCPM vertical cross section illustrating the voltage-induced transition from (a) isolated fingers coexisting with homeotropic state to (f) periodically modulated TIC and then to (g) a uniform TIC. The fingers gradually widen (b)–(e) and then merge in order to form the modulated TIC (f). The polarization of the FCPM probe light marked by “P” is normal to the pictures in (a). The applied voltages are indicated, the confinement ratio is $\rho = 0.9$.

therefore, present only the diagrams corresponding to the largest ρ values at which fingers do not appear for given surface rubbing conditions, see Fig. 7. On the other hand, voltage modulation could be a way to study the stability of different parts of the diagram in the ρ, U plane and deserves

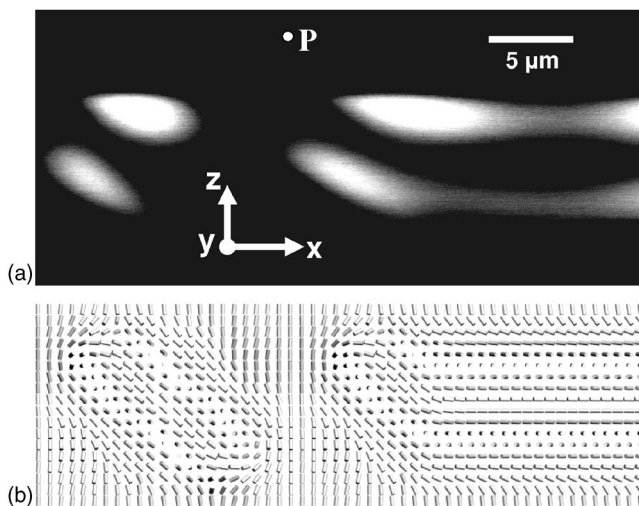


FIG. 12. FCPM cross section (a) and reconstructed director structure (b) illustrating the CF expanding into TIC. The polarization of the FCPM probe light marked by “P” is along y , normal to the picture in (a).

to be explored in more detail; we leave this for forthcoming publications. Finally, to understand the diagrams and transitions explored in this section, it is important to know the director fields that are behind different textures; this will be explored in Sec. III B.

B. Director structures

1. Spatially homogeneous twisted structures, umbilics, and inversion walls

In this section, we take advantage of the FCPM and study the director field $\hat{n}(x, y, z)$ in the vertical cross sections (i.e., along the z axis, normal to the cell substrates) of the cholesteric structures. This is important as, for example, in the TIC, \hat{n} varies only along z and not in the plane of a cell. The TIC, observed above the $V0$ and $V02$ lines in the phase diagrams [Figs. 1, 4, and 7] can be visualized as having \hat{n} rotating with distance from the cell wall on a cone whose axis is along z ; the half angle of this cone varies from $\theta=0$ at the substrates to θ_{\max} in the middle plane of a cell ($\theta_{\max} < \pi/2$), see Fig. 8. FCPM reveals that the in-plane twist of the director in the TIC depends on ρ . For small $\rho \approx 0$, the TIC contains practically no in-plane twist. When $\rho \approx 1/2$, the in-plane twist at high U reaches π , see Figs. 8(a) and 8(c). Finally, when $\rho \approx 1$, the twist of the TIC structure at high U can reach 2π , see Figs. 8(b) and 8(d). The maximum in-plane twist at high U is $\approx 2\pi\rho$; we stress that the twist of TIC depends not only on ρ , but also on U . In addition, for the cells with rubbed homeotropic plates, the in-plane twist is affected by the rubbing direction. For example, the reentrant TIC in the rubbed cells of $0.5 < \rho < 0.75$ has twist $\approx \pi$ at small U just above the $V0$ and the twist close to 2π at high voltages $U > 4V_{rms}$. If both of the homeotropic substrates are rubbed, the natural twist of the TIC structure may or may not be compatible with the tilted easy axes at the confined substrates. Since the amount of twist in the TIC depends both on ρ and U , it is impossible to match tilted homeotropic boundary conditions to a broad range of ρ and U . However, since the in-plane anchoring is weak, the effect of rubbing on the twist in TIC is not as strong as in the case of planar cells.

The FCPM also allows us to probe the defects that appear in TIC. We confirm that the defects with four brushes [Fig. 2(f)] are umbilics of strength ± 1 [12] rather than disclinations with singular cores. We also verify that the umbilics are caused by degeneracy of director tilt when U is applied; such degeneracy is eliminated by rubbing, see Fig. 3(a). Within TIC, we also observe IWs [27,41]. The appearance of these walls was previously attributed to a variety of factors, such as flow of liquid crystal, hydrodynamic instabilities, alignment induced at the edges of the sample, and others [27,41]. FCPM observations indicate that in the presence of spacers with perpendicular anchoring, the IWs appear at the particles when U above the threshold for homeotropic-TIC transition is applied. This is believed to be caused by director distortions in the vicinity of the particles [27,41]. When the confinement ratio is $0.5 < \rho < 0.75$, the distorted TIC with umbilics, disclinations, and IWs is replaced by CFs with the spacers serving as nucleation sites for the fingers, see Fig. 6.

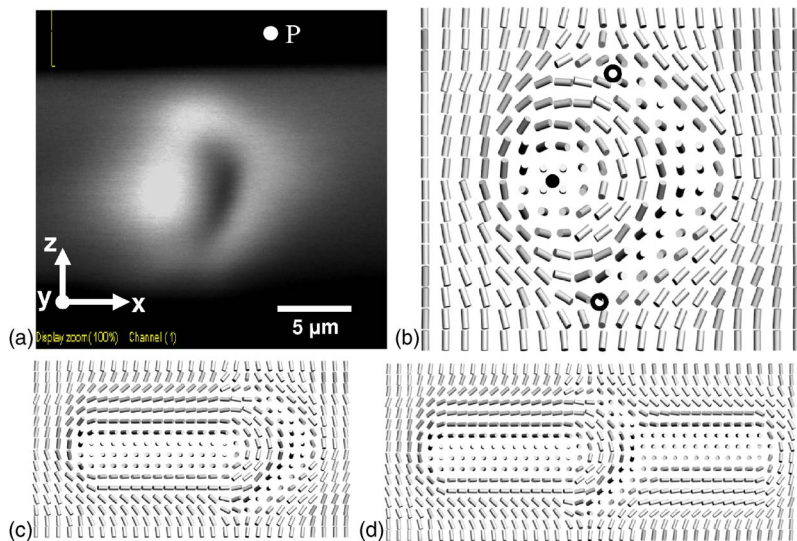


FIG. 13. (Color online) FCPM cross section (a) and reconstructed director structure (b) of CF2 finger; the CF2 can expand in one (c) or two in-plane directions (d) forming TIC. The nonsingular λ disclinations are marked by circles in (b); the open circles correspond to the $\lambda^{-1/2}$ disclinations and the solid circle corresponds to the λ^{+1} disclination. The FCPM polarization is normal to the picture in (a).

2. Fingers structures; nonsingular fingers of CF1 type

Fingers structures have translational invariance along their axes (y direction) and can be observed as isolated between $V3$ and $V0$ or periodically arranged between $V0$ and $V01$ boundary lines, see Figs. 1, 4, and 7 (see Sec. III A for details). We again take advantage of FCPM by visualizing the vertical cross sections and then reconstruct the director field directly from the experimental data. To describe the results, we use the CFs classification of Oswald *et al.* [15]. The finger of CF1 type is the most frequently observed in cells with vertical as well as slightly tilted alignment, see Fig. 9. CF1 is isolated and coexisting with the homeotropic untwisted structure between $V3$ and $V0$ and is a part of the spatially periodic pattern between $V0$ and $V01$ lines, see Figs. 1, 4, and 7. The reason for abundance of CF1, is that it can form from TIC by continuous transformation of the director field above the $V0$ line and it also can easily nucleate from homeotropic untwisted structure below the $V0$ boundary line, see Figs. 1, 4, and 7 [15].

The director structure of CF1 reconstructed from the FCPM vertical cross section (Fig. 9) is in a good agreement with the results of computer simulations [15,17–20]. In the CF1, the axis of cholesteric twist is tilted away from the cell normal z , see Fig. 9; the in-plane twist in direction perpendicular to the finger in the middle of a cell is 2π . The isolated CF1s that are separated from each other by large regions of homeotropic texture [Fig. 2(a)] assume random tilt directions. The width of an isolated CF1 is somewhat larger than d ; this is in a good agreement with computer simulations of Gil [17]. CF1 is nonsingular in $\hat{\mathbf{n}}$ (i.e., the spatial changes of $\hat{\mathbf{n}}$ are continuous and $\hat{\mathbf{n}}$ can be defined everywhere within the structure) as the twist is accompanied with escape of $\hat{\mathbf{n}}$ into the third dimension along its center line. An isolated CF1 can be represented as a quadrupole of the nonsingular λ disclinations, two of strength $+1/2$ and two of strength $-1/2$, as shown in Fig. 9(b). The λ disclinations, with core size of the order of p , cost much less energy than the disclinations with singular cores [13]. The pair of disclinations $\lambda^{+1/2}\lambda^{-1/2}$ introduces a 2π twist at one homeotropic substrate; this 2π twist is then terminated by introducing

another $\lambda^{+1/2}\lambda^{-1/2}$ pair in order to satisfy the homeotropic boundary conditions at another substrate, see Fig. 9(b). A segment of an isolated CF1 has different ends; one is rounded while the another is pointed. Behavior of these ends is different during growth; the pointed end remains stable, while the rounded end continuously splits, as is also discussed in Ref. [26].

The FCPM vertical cross section, Fig. 10, reveals details of CF1 tiling into periodically arranged structures that are observed above $V0$ line, see Figs. 1, 4, and 7. When U or ρ are relatively large, the CF1 fingers are close to each other so that the homeotropic regions in between cannot be clearly distinguished. The tilt of the helical axis in the periodic CF structures is usually in the same direction, see Fig. 10. A possible explanation is that the elastic free energy is minimized since the structure of unidirectionally tilted CFs is essentially space filling. On rare occasions, the tilt direction of neighboring CF1s is opposite. Upon increasing U , the width of fingers originally separated by homeotropic regions [Fig. 11(a)] gradually increases [Figs. 11(b)–11(e)]; the fingers then merge to form a periodically modulated TIC [Fig. 11(f)]. Finally, at high applied voltages, the transition to uniform TIC is observed, see Fig. 11(g). The details of transformation of periodically arranged fingers into the in-plane homogeneous TIC via the modulated (undulating) twisted structure were not known before and would be difficult to grasp without FCPM. TIC can also be formed by expanding one of the CF1s; the structure of coexisting fingers and TIC contains only λ disclinations nonsingular in $\hat{\mathbf{n}}$ again demonstrating the natural tendency to avoid singularities, see Fig. 12. Periodically arranged CF1s slowly (depending on rubbing, U and ρ ; usually up to 1s) appear from TIC if U is between $V0$ and $V01$, and quickly disappear (in less than 50 ms) if U is increased above $V02$. This allowed us to use the amplitude-modulated voltage driving schemes in combination with rubbing and obtain finger-free TIC up to $\rho \approx 0.8$ (Sec. III A 3), as needed for applications of TIC in the electrically driven light shutters, intensity modulators, eye-wear with tunable transparency, displays, etc. [1,5,6,8].

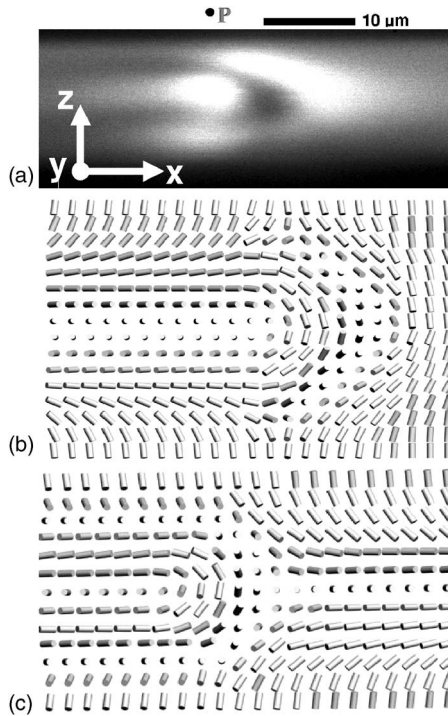


FIG. 14. FCPM cross section (a) and reconstructed director structures (b), (c) formed between the parts of a cell with different in-plane twist and helical axis along the z : (b) TIC with $\approx\pi$ twist, coexisting with homeotropic untwisted state and separated by CF2-like structure with two nonsingular $\lambda^{-1/2}$ disclinations; (c) TIC with $\approx 2\pi$ twist coexisting with TIC with $\approx\pi$ twist. The FCPM polarization marked by “P” is normal to the picture in (a).

3. Fingers of CF2, CF3, and CF4 types containing defects, T junctions of fingers

Another type of fingers is CF2 (Fig. 13), which is observed for vertical as well as slightly tilted alignment in the same parts of the diagram as CF1 (Figs. 1, 4, and 7). However, in contrast to the case of nonsingular CF1, a segment of CF2 has point defects at its ends. Because of this, CF2 does not nucleate from the homeotropic or TIC structures as easily as CF1 and normally dust particles, spacers, or irregularities are responsible for its appearance. Therefore, fingers of CF2 type (Fig. 13) are found less frequently than CF1. Using FCPM, we reconstruct the director structure in the vertical cross section of CF2, see Fig. 13; the experimental result resembles the one obtained in computer simulations by Gil and Gilli [22], proving the latest model of CF2 [15,22] and disproving the earlier ones [23]. Within the CF2 structure, one can distinguish the nonsingular λ^{+1} disclination in the central part of the cell and two half-integer $\lambda^{-1/2}$ disclinations in the vicinity of the opposite homeotropic substrates. The total topological charge of the CF2 is conserved, similarly to the case of CF1. Polarizing microscopic observations show that unlike in CF1-type fingers, the ends of CF2 segments have a similar appearance. FCPM reveals that the point defects (of strength 1) at the two ends have different locations being closer to the opposite substrates of a cell. Unlike the CF1 structure, CF2 is not invariant by π rotation around the y axis along the finger, as also can be seen from

the FCPM cross section, see Fig. 13. Different symmetries of CF1 and CF2 are responsible for their different dynamics under the electric field [15,22]. This, along with computer simulations, allowed Gil and Gilli [22] to propose the model of CF2. Our direct imaging using FCPM unambiguously proves that this model is correct, see Fig. 13(b).

The isolated CF2 fingers (coexisting with homeotropic state) expand, when $U \gtrsim 2.1 V_{rms}$ is applied, see Figs. 13(c) and 13(d). The structures with nonsingular λ disclinations often separate the parts of a cell with a different twist, see Fig. 14; they resemble the structures of thick lines that are observed in Grandjean-Cano wedges with planar surface anchoring [34,37]. The appearance of these lines in homeotropic cells is facilitated by sample thickness variations and spacers. The width of CF2 coexisting with the homeotropic state is usually the same or somewhat (up to 30%) smaller than CF1; this can be seen in Fig. 15 showing a T junction of the CF1 and CF2 fingers. Even though CF1 and CF2 have a similar appearance under a polarizing microscope [15], FCPM allows one to clearly distinguish these structures. Note also the tendency to avoid singularities in \hat{n} evidenced by the reconstructed structure of the T junction, see Fig. 15(b).

The metastable cholesteric fingers of CF3 type (Fig. 16) occur even less frequently than CF2s. The director structure of this finger was originally proposed by Cladis and Kleman [16]. In polarizing microscopy observations, the width of CF3 fingers is about half of that in CF1 and CF2. The reconstructed FCPM structure of CF3 indicates that the director \hat{n} rotates through only π along the axis perpendicular to the finger (x axis). This differs from both CF1 and CF2, which both show a rotation of \hat{n} through 2π . Two twist disclinations of opposite signs near the substrates allow the cholesteric π twist in the bulk to match the homeotropic boundary conditions, see Fig. 16. The structure of CF3 is singular in \hat{n} ; the disclinations are energetically costly and this explains why CF3 is observed rarely even in the cells with vertical alignment. In cells with rubbed homeotropic substrates CF3 was never observed. This is likely due to the easy axis having the same tilt on both sides of the finger on a rubbed substrate, whereas the π -twisted configuration of CF3 requires director tilt in opposite directions.

The CF4-type metastable finger shown in Fig. 17 is also singular, and is usually somewhat wider than the other CFs. It can be found in all regions of existence of CF1 (Fig. 1), but is very rare and usually is formed after cooling the sample from isotropic phase. CF4 contains two singular disclinations at the same substrate. In the plane of a cell, the director \hat{n} rotates by 2π with the twist axis being along x and perpendicular to the finger. Using the direct FCPM imaging, we reconstruct the director structure of CF4 [Fig. 17(b)], which is in a good agreement with the model of Baudry *et al.* [28]. The bottom part of this finger (Fig. 17) is nonsingular and is similar in this respect to CF1 and CF2; its top part, however, contains two singular twist disclinations. The CF4 structure is observed only in cells with no rubbing. Similar to the case of CF3, the structure of CF4 is not compatible with uniform tilt produced by rubbing of homeotropic substrates. Of the four different fingers structures, CF4 might be the least favorable energetically, since it usually rapidly trans-

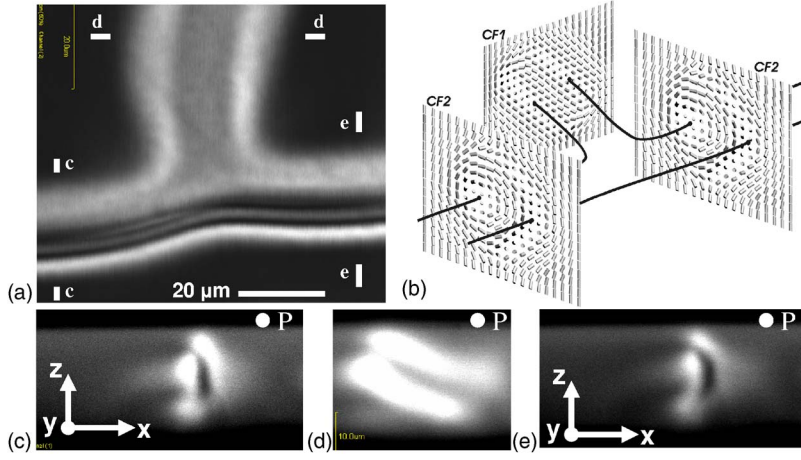


FIG. 15. (Color online) FCPM images and director structure of a T junction of CF1 and CF2: (a) in-plane FCPM section; (b) perspective view of the 3D director field of the T junction; (c)–(e) FCPM cross sections along the lines c - c , d - d , and e - e in part (a). The FCPM cross sections in (c), (e) correspond to CF2 and cross section (d) corresponds to CF1. The FCPM polarization marked by “P” is normal to the pictures in (c)–(e).

forms into CF1 or CF2; less frequently, it also splits into two CF3 fingers. Transformation of other fingers into CF4 was never observed.

IV. DISCUSSION

The system that we study is fairly rich and complicated; some of the structures and transitions can be described analytically while the other require numerical modeling. Below, we first restrict ourselves to translationally uniform structures (i.e., homeotropic and TIC) which can be described analytically. We then discuss the other experimentally observed structures and transitions comparing them to the analytical as well as numerical results available in literature [15,24], as well as our own numerical study of the phase diagram that will be published elsewhere [42]. Finally, we discuss the practical importance of the obtained results on the phase diagrams of director structures.

A. Translationally uniform homeotropic and TIC structures

We represent the director $\hat{\mathbf{n}}$ in terms of the polar angle θ (between the director and the z axis) and the azimuthal angle ϕ (the twist angle); ψ is electric potential. For the TIC configurations, these fields are functions of z only, and the Oseen-Frank free-energy density takes the form

$$\begin{aligned}
 2f = & (K_{11} \sin^2 \theta + K_{33} \cos^2 \theta) \theta_z^2 \\
 & + (K_{22} \sin^2 \theta + K_{33} \cos^2 \theta) \sin^2 \theta \phi_z^2 - K_{22} \frac{4\pi}{p} \\
 & \times \sin^2 \theta \phi_z + K_{22} \frac{4\pi^2}{p^2} - (\varepsilon_{\perp} \sin^2 \theta + \varepsilon_{\parallel} \cos^2 \theta) \psi_z^2,
 \end{aligned} \quad (1)$$

where, K_{11} , K_{22} , and K_{33} are the splay, twist, and bend elastic constants, respectively; ε_{\parallel} , ε_{\perp} are the dielectric constants parallel and perpendicular to $\hat{\mathbf{n}}$, respectively; $\theta_z = d\theta/dz$, $\phi_z = d\phi/dz$, and $\psi_z = d\psi/dz$. The associated coupled Euler-Lagrange equations are

$$\begin{aligned}
 \frac{d}{dz} [(K_{11} \sin^2 \theta + K_{33} \cos^2 \theta) \theta_z] \\
 = \sin \theta \cos \theta \left\{ (K_{11} - K_{33}) \theta_z^2 + [(2K_{22} - K_{33}) \sin^2 \theta \right. \\
 \left. + K_{33} \cos^2 \theta] \phi_z^2 - K_{22} \frac{4\pi}{p} \phi_z - \Delta \varepsilon \psi_z^2 \right\}, \quad (2)
 \end{aligned}$$

$$\frac{d}{dz} \left\{ \sin^2 \theta \left[(K_{22} \sin^2 \theta + K_{33} \cos^2 \theta) \phi_z - K_{22} \frac{2\pi}{p} \right] \right\} = 0, \quad (3)$$

$$\frac{d}{dz} [(\varepsilon_{\perp} \sin^2 \theta + \varepsilon_{\parallel} \cos^2 \theta) \psi_z] = 0, \quad (4)$$

with associated boundary conditions $\theta(0) = \theta(d) = 0$; $\phi(0)$, $\phi(d)$ are undefined; and $\psi(0) = 0$, $\psi(d) = U$. Dielectric anisotropy is negative for the studied material, $\Delta \varepsilon = \varepsilon_{\parallel} - \varepsilon_{\perp} < 0$. Representative solutions of these equations are plotted in Fig. 18 and describe how $\theta(z)$, $\phi(z)$, and $\psi(z)$ vary across the cell.

Equations (3) and (4) above admit first integrals,

$$\phi_z = \frac{K_{22}}{K_{22} \sin^2 \theta + K_{33} \cos^2 \theta} \frac{2\pi}{p} \quad (5)$$

and

$$(\varepsilon_{\perp} \sin^2 \theta + \varepsilon_{\parallel} \cos^2 \theta) \psi_z = \frac{U}{\int_0^d \frac{1}{\varepsilon_{\perp} \sin^2 \theta + \varepsilon_{\parallel} \cos^2 \theta} dz}, \quad (6)$$

which allow us to express the free energy in terms of the tilt angle θ only

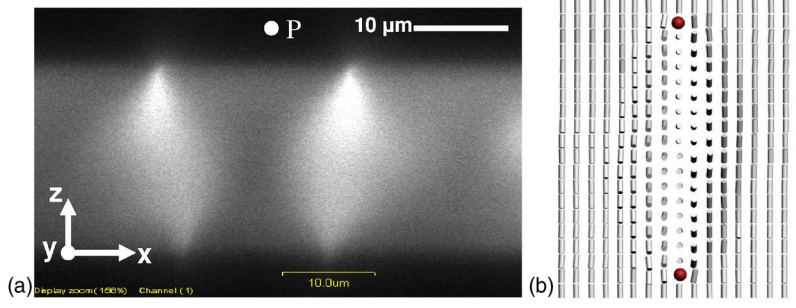


FIG. 16. (Color online) FCPM cross section (a) and reconstructed director structures (b) of CF3 finger. The FCPM polarization marked by “P” is normal to the picture in (a). Two CF3s can be seen in (a); the director structure of only one CF3 is shown in (b). The singular disclinations at the two substrates are marked by circles in (b).

$$\mathcal{F}[\theta] = \frac{1}{2} \int_0^d \left[(K_{11} \sin^2 \theta + K_{33} \cos^2 \theta) \theta_z^2 + \frac{K_2 K_3 \cos^2 \theta}{K_{22} \sin^2 \theta + K_{33} \cos^2 \theta} \frac{4\pi^2}{p^2} \right] dz - \frac{1}{2} U^2 \left[\int_0^d \frac{1}{\varepsilon_{\perp} \sin^2 \theta + \varepsilon_{\parallel} \cos^2 \theta} dz \right]^{-1}. \quad (7)$$

This is similar to Eq. (3.221) of Ref. [43] (see p. 91), where the splay Fredericksz transition with a coupled electric field is discussed. We expand the free energy in terms of $\theta(z)$ about the undistorted $\theta=0$ homeotropic configuration to obtain

$$\mathcal{F}[\theta] = \frac{1}{2} \left[\frac{4\pi^2 d K_{22}}{p^2} - \frac{\varepsilon_{\parallel} U^2}{d} \right] + \frac{1}{2} \int_0^d \left[K_{33} \theta_z^2 - \left(\frac{\Delta \varepsilon U^2}{d^2} + \frac{4\pi^2 K_{22}^2}{p^2 K_{33}} \right) \theta^2 \right] dz + O(\theta^4). \quad (8)$$

The first term is the free energy of the uniform homeotropic configuration. The second-order term is positive definite if U and ρ are sufficiently small. Ignoring higher order terms, we find that the loss of stability occurs when

$$\frac{4K_{22}^2}{K_{33}^2} \rho^2 + \frac{\Delta \varepsilon}{K_{33} \pi^2} U^2 = 1. \quad (9)$$

Equation (9) is the spinodal ellipse. The homeotropic configuration is metastable with respect to translationally homogeneous perturbations for the ρ and U parameters inside the ellipse (9), which corresponds to the boundary line V_0 , see Figs. 1, 4, and 7. Equation (9) gives the threshold voltage for transition between homeotropic and TIC structures

$$U_{th} = \pi \sqrt{K_{33} / \Delta \varepsilon} \sqrt{1 - 4\rho^2 K_{22}^2 / K_{33}^2}. \quad (10)$$

Equation (10) is in a good agreement with our experimental results described in Sec. III above and with Ref. [40]. The experimental data for boundary line V_0 are well described by Eq. (9) for rubbed and unrudded homeotropic cells, see Figs. 1, 4, and 7. According to the linear stability analysis above, the ellipse in the ρ - U plane (10) defines the limit of metastability of the homeotropic phase: for ρ and U inside this ellipse, the uniform homeotropic configuration is metastable, while outside the ellipse, it is a locally unstable equilibrium. In an idealized cell with infinitely strong homeotropic anchoring and no pretilt, the transition from homeotropic to TIC is a forward pitchfork bifurcation, that is, a second-order transition. For voltages U below the V_0 line (inside the ellipse), the TIC configuration does not exist. On the other hand, when there is a slight tilt of the easy axis, the reflection symmetry is broken. The pitchfork is unfolded into a smoother transition, i.e., the transition becomes supercritical

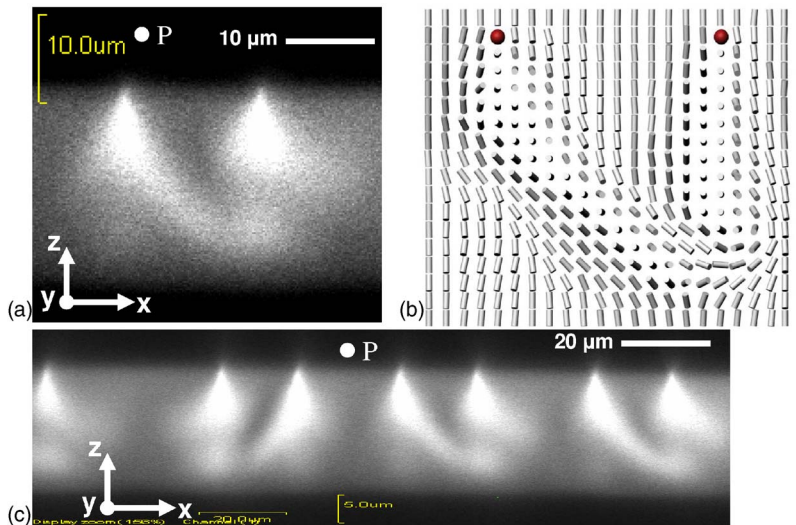


FIG. 17. (Color online) FCPM cross sections (a), (c) and reconstructed director structure (b) of the CF4 fingers. The FCPM polarization is along y in (a), (c). The singular disclinations at one of the substrates are marked by circles in (b). The CF4s in (c) have singular disclinations at the same substrate.

and the precise transition threshold is not well defined. The experimentally observable artifact of this is the somewhat blurred transition, which is described in Sec. III A 2, for the cells with rubbing and resembles a similar effect in planar cells with small pretilt [39].

The above analysis allows one to understand the dependence of the total in-plane twist of TIC on ρ and U that was described in Sec. III B 1. The first integral (5) gives the tilt-dependence of the local twist rate. The total twist across a cell of thickness d is

$$\Delta\phi = \frac{2\pi}{\rho} \int_0^d \frac{K_{22}}{K_{22} \sin^2 \theta + K_{33} \cos^2 \theta} dz. \quad (11)$$

For the AMLC-0010 material with $K_{22}/K_{33} \approx 0.42$ for given ρ the total twist $\Delta\phi$ can be varied

$$0.42 * 2\pi\rho < \Delta\phi < 2\pi\rho, \quad (12)$$

by changing U . $\Delta\phi$ approaches the lower limit for relatively small U that are just above U_{th} and $\theta \approx 0$ and the upper limit for $U \gg U_{th}$ and $\theta \approx \pi/2$. This analysis is in a good agreement with the FCPM images of the vertical cross sections of TIC for different ρ , as described in Sec. III. Finally, knowledge of $\Delta\phi$ variation with changing U is important for the practical applications of TIC as it will be discussed below.

B. Other structures and transitions of the phase diagram

Modeling of transitions associated with CFs, in which $\hat{\mathbf{n}}$ is a function of two coordinates, is more complicated than in the case of TIC. Ribière, Pirkel, and Oswald [24] obtained complete phase diagram in calculations assuming a simplified model of a cholesteric finger. This theoretical diagram qualitatively resembles our experimental result for the cells with vertical alignment, see Fig. 1. We explored the phase diagram using two-dimensional (2D) numerical modeling in which the equilibrium structure of the CFs and the equilibrium period of periodically arranged fingers are determined from energy minimization in a self-consistent way and the nonlocal field effects are taken into account [42]. The numerical phase diagrams show a good quantitative agreement with the experimental results presented here, predicting even the reentrant behavior of TIC that we experimentally obtain for cells with rubbed substrates (Sec. III A 2). Presentation of these results requires detailed description of numerical modeling and will be published elsewhere [42]. Therefore, we only briefly discuss the qualitative features of the phase diagrams shown in Figs. 1, 4, and 7 in the light of the previous theoretical studies [15,24] and also summarize the new experimental results below.

The important feature of the studied diagram is that the nematic-cholesteric transition changes order: it is second order for $0 < \rho < \rho_{triple}$ and first order for $\rho > \rho_{triple}$ (Fig. 1), in agreement with Refs. [15,24]. The phase diagram has a triple point at $\rho = \rho_{triple}$, where V0 and V01 meet and the untwisted homeotropic texture coexists with two twisted structures, TIC and periodically arranged CFs, see Figs. 1, 4, and 7. For vertical alignment, the direct voltage-driven

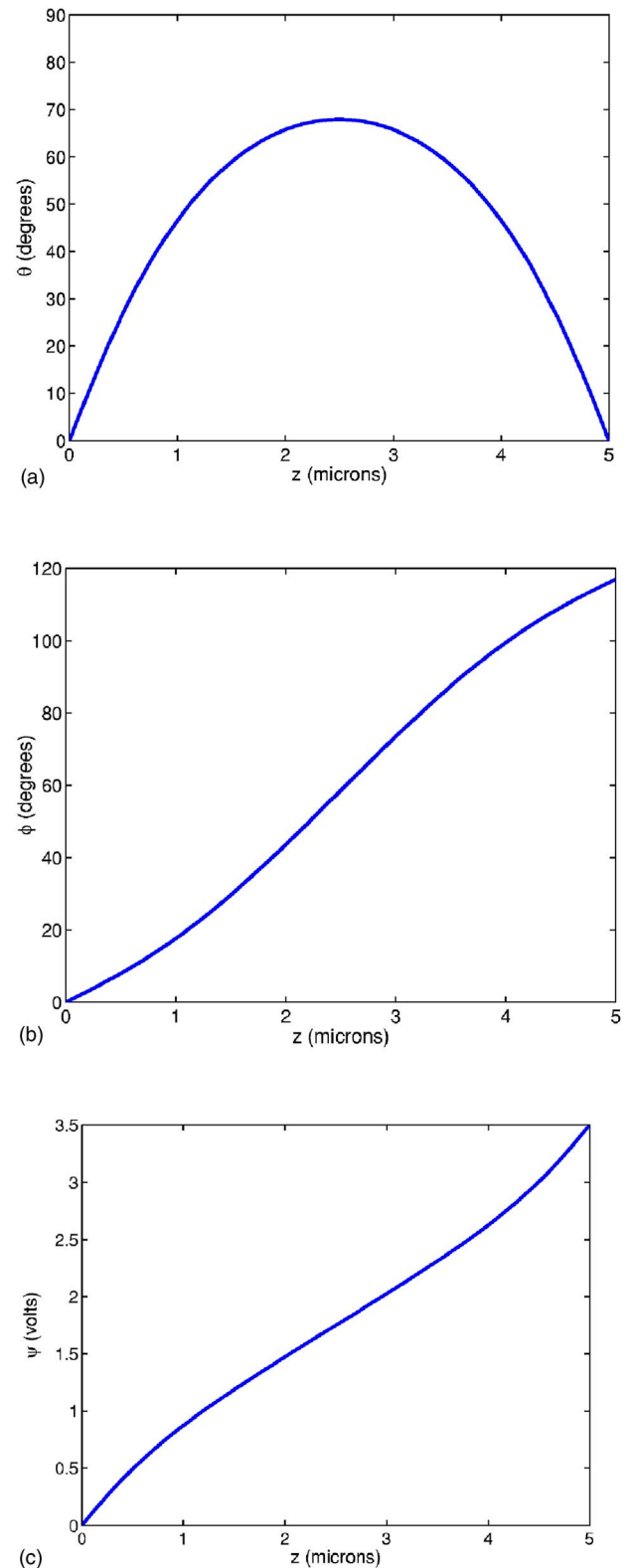


FIG. 18. (Color online) A representative TIC equilibrium configuration obtained as numerical solution of Eqs. (2)–(4): (a) tilt angle θ , (b) twist angle ϕ , (c) electric potential ψ . The material parameters used in the calculations were taken for the AMLC-0010 host doped with ZLI-811, $d=5 \mu\text{m}$, $\rho=0.5$, $U=3.5 V_{rms}$.

homeotropic-TIC transition is observed at small $\rho \lesssim 0.5$. Structures of isolated CFs and periodically arranged CFs occur for $0.5 \lesssim \rho < 1$ and intermediate U between the homeotropic state and TIC. The theoretical analysis of Ref. [24] allows one to determine ρ corresponding to the tricritical and triple points in the phase diagrams. Solving the equations given in Ref. [24] numerically [44] and using the material parameters of the AMLC-0010 host doped with the chiral agent ZLI-811, we find ρ corresponding to the triple and tricritical points: $\rho_{\text{triple}}=0.816$ and $\rho_{\text{tricritical}}=0.861$. These values are somewhat larger than ρ_{triple} and $\rho_{\text{tricritical}}$ determined experimentally for the cells with vertical alignment, (Figs. 1, 4, and 7), as also observed in [24] for other CLCs. The calculated ρ_{triple} and $\rho_{\text{tricritical}}$ are closer to the experimental ones in the case of rubbed substrates; this may indicate the possible role of umbilics and IWs in the TIC, which were not taken into account in the model [24] (umbilics and IWs are nucleation sites for fingers and may also increase elastic energy of TIC). Agreement is improved when phase diagrams are obtained using 2D numerical modeling [42]. An interesting new finding revealed by the FCPM is that upon increasing U , the periodically arranged fingers merge with each other forming modulated (undulating) TIC that is observed in a narrow voltage range between the structures of TIC and periodically arranged CFs, see Figs. 1, 4, and 7. We also find that the phase boundaries can be shifted in a controlled way by the rubbing-induced tilt ($< 2^\circ$) of easy axis from the vertical direction, by introducing particles that become nucleation sites for CFs, as well as by using different amplitude-modulated voltage schemes.

A novel and unexpected result is the reentrant behavior of TIC in the rubbed cells with $0.6 \lesssim \rho \lesssim 0.75$, which, however, disappears if nucleation sites are present. FCPM allows us to directly and unambiguously determine the 3D director structures corresponding to different parts of the phase diagram. In particular, we unambiguously reconstruct the structures of four types of CFs. In all parts of diagrams corresponding to stability or metastability of CFs, the fingers of CF1 type are the most frequently observed. CF2 fingers are less frequent; the metastable CF3 and CF4 are very rare. Such findings indicate that fingers of CF1 type have the lowest free energy out of four fingers; this is consistent with the reconstruction of the structure of CF1, which is nonsingular in \hat{n} . It is also natural that CF2 with singular point defects and especially metastable CF3 and CF4 with singular line defects are less frequently observed. In the case of rubbed homeotropic substrates, only CF1 and CF2 are observed; whereas, CF3 and CF4 never appear because the rubbing-induced tilting of the easy axis at one or both substrates contradicts with their symmetry.

C. Control of phase diagrams to enable practical applications

The combination of rubbing and amplitude-modulated voltage driving allows one to suppress appearance of fingers up to high $\rho \approx 0.75$ (compare Fig. 1 and Fig. 7). This is a valuable finding for many practical applications such as eyeglasses with voltage-tunable transparency and light shutters [5], bistable [8] and inverse twisted nematic displays [6], etc.

In these applications of the homeotropic-TIC transition, it is important to have a broad range of well controlled total twist $\Delta\phi$ in the finger-free TIC. The broad range of voltage-tuned $\Delta\phi$ allows one to control optical phase retardation in the displays and electro-optic devices [6,8] as well as light absorption when the dye-doped CLC is used in the tunable eyeglasses and light shutters [5]. A very subtle tilt of easy axis from the vertical direction not only makes the director twist in TIC vary in a controlled way but also suppresses the appearance of fingers, IWs, and umbilics, see Figs. 3–7. Slow appearance of fingers from TIC and untwisted homeotropic states allowed us to magnify the effect of rubbing via using amplitude-modulated voltage schemes and suppress appearance of fingers up to even higher ρ , see Fig. 7. For example, we can control $\Delta\phi=55^\circ-270^\circ$ in the finger-free TIC. Even stronger effects of rubbing and voltage modulation can be expected if the tilt of the easy axis is increased. This might be implemented by using the approach recently developed by Huang and Rosenblatt [45], in which case, a tilt of easy axis up to 30° could be achieved. On the other hand, when constructing cells for all of the above applications of tightly twisted TIC, it is important to remember about the effect of particles, which become nucleation sites for fingers and can cause their appearance at lower ρ . Such particles are often used as spacers to set cell thickness and it is, therefore, important to either avoid their usage or limit (optimize) their concentration in order to obtain finger-free TIC.

The finding that fingers align along the rubbing direction (Sec. III A) may enable the use of periodically arranged CFs in switchable diffraction gratings with the diffraction pattern corresponding to the field-on state. The spatial periodicity and the diffraction properties of such gratings can be easily controlled by selecting proper pitch p and cell gap d , which can be varied from submicron to tens of microns. Our preliminary study shows that the grating periodicity can be changed in range $1-50 \mu\text{m}$. More detailed studies of the cholesteric diffraction gratings based on voltage-induced well-oriented pattern of CFs will be published elsewhere.

V. CONCLUSIONS

The major findings of this work are threefold: (1) we obtained phase diagram of CLC structures as a function of confinement ratio $\rho=d/p$ and voltage U for different extra parameters such as rubbing, voltage driving, presence of nucleation sites; (2) we enabled new applications of finger-free tightly twisted TIC and well-oriented fingers; (3) we unambiguously deciphered 3D director fields associated with different structures and transitions in CLCs using FCPM. In the phase diagram, the direct homeotropic-TIC transition upon increasing U was observed for $\rho \lesssim 0.5$; the analytical model of this transition is in a very good agreement with the experiment. Structures of isolated and periodically arranged fingers were found at $0.5 \lesssim \rho < 1$ and intermediate U between the homeotropic and TIC phases. We observed the reentrant behavior of TIC in the rubbed cells of $0.6 \lesssim \rho \lesssim 0.75$ for which the following sequence of transitions has been observed upon increasing U : (1) homeotropic untwisted (2)

TIC, (3) periodically arranged fingers, (4) TIC with larger in-plane twist. The reentrant behavior of TIC is also observed in our numerical study of the phase diagram that will be published elsewhere [42]. The reentrant TIC disappears if nucleation sites are present or amplitude-modulated driving schemes are used. Rubbing also eliminates nonuniform in-plane structures such as umbilics and inversion walls that otherwise are often observed in TIC and also influence the phase boundary lines. The lowest ρ for which periodically arranged fingers start to be observed upon increasing U can be shifted for up to 0.3 toward higher ρ values by rubbing and/or voltage driving schemes. The FCPM allowed us to unambiguously determine and confirm the latest director models [15] for the vertical cross sections of four types of CFs (CF1–CF4), while disproving some of the earlier models [23]. The CF1-type fingers are observed in all regions of the phase diagrams where the fingers are either stable or metastable; other fingers appear in the same parts of the diagram but less frequently. For the rubbed cells, only two types of CFs (CF1 and CF2) are observed, which align along the

rubbing direction. The new means to control structures in CLCs are of importance for potential applications, such as switchable gratings based on periodically arranged CFs and eyewear with tunable transparency based on TIC.

ACKNOWLEDGMENTS

The work is part of the AlphaMicron/TAF collaborative project “Liquid Crystal Eyewear,” supported by the state of Ohio and AlphaMicron, Inc. I.I.S. and O.D.L. acknowledge the support of the NSF, Grant No. DMR-0315523. I.I.S. acknowledges the support of the Institute for Complex and Adaptive Matter. E.C.G. acknowledges support under NSF Grant No. DMS-0107761, as well as the hospitality and support of the Department of Mathematics at the University of Pavia (Italy) and the Institute for Mathematics and its Applications at the University of Minnesota, where part of work was carried out. We are grateful to M. Kleman, L. Longa, Yu. Nastishin, and S. Shiyonovskii for discussions.

-
- [1] L. M. Blinov and V. G. Chigrinov, *Electrooptic Effects in Liquid Crystal Materials* (Springer, New York, 1994).
- [2] P. F. McManamon, T. A. Dorschner, D. L. Corkum, L. J. Friedman, D. S. Hobbs, M. Holz, S. Liberman, H. Q. Nguyen, D. P. Resler, R. C. Sharp, and E. A. Watson, *Proc. IEEE* **84**, 268 (1996).
- [3] P. Palffy-Muhoray, *Nature (London)* **391**, 745 (1998).
- [4] D-K. Yang, X-Y. Huang, and Y-M. Zhu, *Annu. Rev. Mater. Sci.* **27**, 117 (1997).
- [5] P. Palffy-Muhoray, T. Kosa, and B. Taheri, Variable light attenuating dichroic dye guest-host device, PCT Int. Appl. WO 9967681 (1999); B. Taheri, P. Palffy-Muhoray, T. Kosa and D. L. Post., *Proc. SPIE* **4021**, 114 (2002).
- [6] J. S. Patel and G. B. Cohen, *Appl. Phys. Lett.* **68**, 3564 (1996).
- [7] B. I. Senyuk, I. I. Smalyukh, and O. D. Lavrentovich, *Opt. Lett.* **30**, 349 (2005).
- [8] J. S. Hsu, B-J. Liang, and S-H. Chen, *Appl. Phys. Lett.* **85**, 5511 (2004).
- [9] F. A. Munoz, P. Palffy-Muhoray, and B. Taheri, *Opt. Lett.* **26**, 804 (2001).
- [10] M. F. Moreira, I. C. S. Carvalho, W. Cao, C. Bailey, B. Taheri, and P. Palffy-Muhoray, *Appl. Phys. Lett.* **85**, 2691 (2004).
- [11] J. Schmidtke, W. Stille, and H. Finkelmann, *Phys. Rev. Lett.* **90**, 083902 (2003).
- [12] P. G. de Gennes and J. Prost, *The Physics of Liquid Crystals* (Clarendon, Oxford, 1993).
- [13] M. Kleman and O. D. Lavrentovich, *Soft Matter Physics: An Introduction* (Springer, New York, 2003).
- [14] O. D. Lavrentovich and M. Kleman, in *Chirality in Liquid Crystals*, edited by C. Bahr and H. Kitzerow (Springer, New York, 2001).
- [15] P. Oswald, J. Baudry, and S. Pirkel, *Phys. Rep.* **337**, 67 (2000).
- [16] P. E. Cladis and M. Kleman, *Mol. Cryst. Liq. Cryst.* **16**, 1 (1972).
- [17] L. Gil, *J. Phys. II* **5**, 1819 (1995).
- [18] S. V. Shiyonovskii, I. I. Smalyukh, and O. D. Lavrentovich, in *Defects in Liquid Crystals: Computer Simulations, Theory and Experiments*, edited by O. D. Lavrentovich, P. Pasini, C. Zannoni, and S. Žumer, NATO Science Series 43, (Kluwer Academic, Dordrecht, 2001).
- [19] M. J. Press and A. S. Arrott, *J. Phys. (France)* **37**, 387 (1976).
- [20] M. J. Press and A. S. Arrott, *Mol. Cryst. Liq. Cryst.* **37**, 81 (1976).
- [21] M. J. Press and A. S. Arrott, *J. Phys. (France)* **39**, 750 (1978).
- [22] L. Gil and J. M. Gilli, *Phys. Rev. Lett.* **80**, 5742 (1998).
- [23] J. Baudry, S. Pirkel, and P. Oswald, *Phys. Rev. E* **57**, 3038 (1998); **59**, 5562 (1999).
- [24] P. Ribiere, S. Pirkel, and P. Oswald, *Phys. Rev. A* **44**, 8198 (1991).
- [25] O. S. Tarasov, A. P. Krekhov, and L. Kramer, *Phys. Rev. E* **68**, 031708 (2003).
- [26] P. Oswald, J. Baudry, and T. Rondepierre, *Phys. Rev. E* **70**, 041702 (2004).
- [27] J. M. Gilli, S. Thiberge, A. Vierheilg, and F. Fried, *Liq. Cryst.* **23**, 619 (1997).
- [28] J. Baudry, S. Pirkel, and P. Oswald, *Phys. Rev. E* **57**, 3038 (1998).
- [29] F. Lequeux, P. Oswald, and J. Bechhoefer, *Phys. Rev. A* **40**, 3974 (1989).
- [30] T. Ishikawa and O. D. Lavrentovich, *Phys. Rev. E* **60**, R5037 (1999).
- [31] I. I. Smalyukh, S. V. Shiyonovskii, and O. D. Lavrentovich, *Chem. Phys. Lett.* **336**, 88 (2001).
- [32] B. L. van Horn and H. Henning Winter, *Appl. Opt.* **40**, 2089 (2001); T. J. Scheffer and J. Nehring, *J. Appl. Phys.* **48**, 1783 (1977).
- [33] M. Born and E. Wolf, *Principles of Optics* (Cambridge University Press, Cambridge, 1999).
- [34] I. I. Smalyukh and O. D. Lavrentovich, *Phys. Rev. E* **66**, 051703 (2002).

- [35] T. Kosa, V. H. Bodnar, B. Taheri, and P. Palffy-Muhoray, *Mol. Cryst. Liq. Cryst. Sci. Technol., Sect. A* **369**, 129 (2001).
- [36] W. E. Ford and P. V. Kamat, *J. Phys. Chem.* **91**, 6373 (1987).
- [37] I. I. Smalyukh and O. D. Lavrentovich, *Phys. Rev. Lett.* **90**, 085503 (2003).
- [38] W. H. de Jeu, *Physical Properties of Liquid Crystalline Materials* (Gordon and Breach, New York, 1979).
- [39] P. Yeh and C. Gu, *Optics of Liquid Crystal Displays* (Wiley, New York, 1999).
- [40] K. A. Crandall, M. R. Fisch, R. G. Petschek, and C. Rosenblatt, *Appl. Phys. Lett.* **64**, 1741 (1994).
- [41] P. E. Cladis, W. van Saarloos, P. L. Finn, and A. R. Kortan, *Phys. Rev. Lett.* **58**, 222 (1987).
- [42] E. C. Gartland, Jr. *et al.* (unpublished).
- [43] I. W. Stewart, *The Static and Dynamic Continuum Theory of Liquid Crystals* (Taylor & Francis, Boca Raton, FL 2004).
- [44] We note that there is a mistake in Eq. (29) of Ref. [15] as it is different from Eq. (14) of Ref. [24].
- [45] Z. Huang and C. Rosenblatt, *Appl. Phys. Lett.* **86**, 011908 (2005).